CHAPTER SEVENTY FOUR

A Finite Element Model for Wind Wave Diffraction

Ove Skovgaard* Lars Behrendt** Ivar G. Jonsson***

Abstract

The applicability of a hybrid finite element model for the calculation of combined diffraction-refraction of small time-harmonic water waves is demonstrated. The model is valid for arbitrary water depths and wave lengths, i.e. it is based on intermediate depth theory (IDT). The model includes arbitrarily varying partial reflection along the boundaries. Superposition of waves (to simulate a spectrum approach) with different incident directions is demonstrated, and CPU-times and core memory requirements are given.

The model is verified and documented with respect to sensitivity of the model parameters in detailed tables, using the classical Homma island on a parabolic shoal. The wave period is here chosen in such a way that a small number of elements (larger than 500 and less than 2,000) is enough to get an accurate solution.

For a new simple, but realistic harbour geometry many detailed and accurate graphical results are given. The wave period (T = 9 sec.) is here chosen so that it is representative for natural wind waves, and the size of the harbour is selected, so that the model gets a fairly large number of elements (of the order 10,000).

1. Introduction

Small-amplitude time-harmonic waves of arbitrary length propagating in an area of varying depth may be described by the mild-slope wave equation. This equation was first derived by Berkhoff (1972). He solved the mild-slope wave equation by using a finite element method based on sources placed along the open boundaries. Chen and Mei (1974) formulated a hybrid finite element model (FEM) based on shallow water theory (SWT). This model was generalized to intermediate depth theory (IDT) by Houston (1981). Houston's hybrid FEM is restricted to full reflection along solid boundaries. In Behrendt and Jonsson (1984) a new derivation of the fundamental functional is presented. This new method includes partially absorbing boundaries and makes it straightforward also to include bottom friction.

In the present paper the hybrid functional by Behrendt and Jonsson (1984) (hereafter denoted by Paper I) is implemented, verified by comparison with exact solutions, and investigated for sensivity of model parameters. The computational requirements and many detailed and accu-

* Ph.D., Assoc. Prof., Laboratory of Applied Mathematical Physics (LAMF), Bldg. 303; ** M.Sc., Postgrad. Stud.; *** Ph.D., Assoc. Prof., Institute of Hydrodynamics and Hydraulic Engineering (ISVA), Bldg. 115,

Technical University of Denmark
DK-2800 Lyngby, Denmark.

rate results are illustrated for a new simple but realistic harbour geometry. In this harbour we demonstrate that partial reflection can be specified arbitrarily varying along solid boundaries (e.g. rubble mound breakwaters). This property is crucial for realistic modelling of wind wave diffraction in harbours. Another crucial property for practical applications is that superposition of waves with different directions and periods is computationally feasible.

2. The Hybrid Finite Element Model and its Implementation

This hybrid FEM is a combination of a simple finite element approach in area A (see Figs. 1 and 2) and a semi-analytical expansion in the outer area R (see Figs. 1 and 2), where we assume a constant water depth.

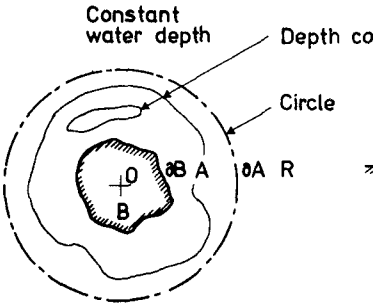

Figure 1. Sketch of model in the horizontally plane, infinite ocean.

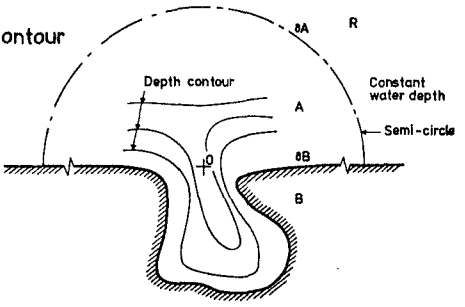

Figure 2. Sketch of model in the horizontally plane, semi-infinite ocean.

Inside the circle or semi-circle ∂A the depth contours can be specified arbitrarily, but the change in depth over a wave length of the water waves has to be moderate. Along the "solid" boundary ∂B energy may be absorbed by specifying an arbitrarily varying absorption coefficient α ($0 \leq \alpha \leq 1$). Thus, $\alpha = 1$ corresponds to full absorption of waves incident at a right angle, and $\alpha = 0$ corresponds to a fully reflecting boundary. The partially absorbing boundary condition is the well-known Eq. (21) in Paper I.

The semi-analytical expansion in the outer area R of constant water depth is a solution to the classical Helmholtz wave equation (which is the constant water depth version of the mild-slope wave equation, see Paper I Eq. (20)) satisfying the Sommerfeld radiation condition (see Paper I Eq. (14)) at infinity. For the infinite ocean in Fig. 1 the expansion is:

$$\phi^S = \sum_{n=0}^{\infty} H_n^{(1)}(kr) \, [\alpha_n \cos(n\theta) + \beta_n \sin(n\theta)] \qquad (1)$$

where ϕ^S is the velocity potential of the scattered wave field (see Paper I Eq. (15)), $H_n^{(1)}$ is the Hankel function of the first kind of order n, k is the wave number, and r and θ are polar co-ordinates in the horizontal plane. The coefficients α_n and β_n are determined by matching this solution with the solution in area A.

For the semi-infinite ocean in Fig. 2 the expansion is the same as in Eq. (1) with $\beta_n \equiv 0$, n = 0, 1, ..., ∞. Now θ equals 0^o or 180^o along the infinite, fully reflecting straight coastline in area R. In the model the expansions are truncated at n = nmax which is an input parameter to the model. The number nmax depends on the desired accuracy of the solution and on the maximum distance r from the origo 0. For the classical Homma island, see Homma (1950), the necessary number nmax has been studied in Appendix I in Skovgaard and Jonsson (1981).

The basic principle in the present finite element method is the minimization of a functional $F_H(\phi)$, see Eq. (44) in Paper I. This minimization is expressed in Eq. (45) in Paper I. The functional is discretisized using finite elements in area A and using the expansion (1) describing ϕ^S along ∂A. The finite elements chosen are simple triangular three-node elements with linear shape functions. This procedure results in a system of complex linear equations with a quadratic banded sparse symmetric coefficient matrix {K}. The maximum semi-bandwidth depends strongly on the chosen numbering of the nodes in the finite element grid. In the pioneering study by Chen and Mei (1974) the semi-bandwidth was also much dependent on the number of nodes along ∂A, and on 'nmax'.

3. An Example of Verification and Sensitivity: Homma's Island

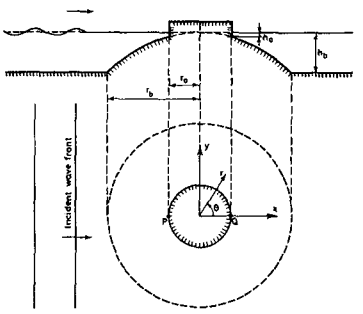

Figure 3. Sketch of an idealized island on a parabolic shoal; (a) vertical; (b) horizontal. r_a = 10,000 m, r_b = 30,000 m, h_b = 4,000 m, $h_a = h_b(r_a/r_b)^2$ = 4,000/9 m.

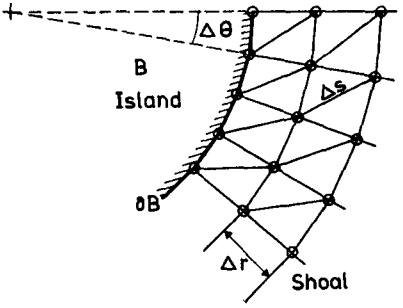

Figure 4. Horizontal sketch of finite element grid over part of the shoal in Fig. 3. The grid covers the shoal for $0^o \leq \theta < 360^o$ and $r_a \leq r \leq r_b$.

As an example from the verification program we have considered the classical Homma island surrounded by a parabolic shoal in an infinite ocean of constant water depth, see Fig. 3, and Jonsson et al. (1976), Table 1 and Eq. (1.1). A detail of the finite element grid is shown in Fig. 4.

The boundary ∂B is fully reflecting in this example. The boundary ∂A has been placed along the outer boundary of the shoal, i.e. area A is

Table I. Text: see next page, top.

	$\theta = 0^\circ$	$\theta = 30^\circ$	$\theta = 60^\circ$	$\theta = 90^\circ$	$\theta = 120^\circ$	$\theta = 150^\circ$	$\theta = 180^\circ$	$\sum\lvert\text{line}\rvert$
	2.3708	1.7663	1.5067	2.6885	3.3686	3.4553	3.4193	
$(A/A_i)_{r=r_a}$	-.0324	-.0213	+.0050	-.0176	-.0222	-.0115	-.0050	0.1150
	-.0981	-.0644	+.0202	-.0424	-.0553	-.0234	-.0042	0.3080
	151.69	134.42	60.33	16.40	355.95	341.70	335.92	
$(\varphi^\circ)_{r=r_a}$	-1.30	-1.69	-0.92	-0.56	-0.58	-0.45	-0.28	5.78
	-4.00	-5.28	-2.96	-1.67	-1.66	-1.21	-0.69	17.47
	1.8330	1.2805	1.0478	1.8636	1.9754	1.6535	1.4924	
$(A/A_i)_{r=2r_a}$	-.0138	-.0064	+.0041	-.0079	-.0071	+.0003	+.0040	0.0436
	-.0342	-.0127	+.0132	-.0177	-.0134	+.0069	+.0164	0.1145
	170.97	152.55	64.80	18.54	353.78	332.71	322.61	
$(\varphi^\circ)_{r=2r_a}$	-0.81	-1.05	-0.35	-0.42	-0.59	-0.52	-0.34	4.08
	-2.33	-2.91	-0.83	-1.08	-1.57	-1.44	-1.03	11.19
	1.5372	0.9995	0.8037	1.3281	0.9573	0.4871	0.4960	
$(A/A_i)_{r=3r_a}$	+.0028	+.0063	+.0058	+.0047	+.0098	+.0092	+.0022	0.0408
	+.0077	+.0180	+.0171	+.0135	+.0273	+.0272	+.0083	0.1191
	195.95	176.09	70.91	21.01	344.19	282.12	242.10	
$(\varphi^\circ)_{r=3r_a}$	-0.66	-0.75	+0.06	-0.33	-0.53	+0.45	+0.91	3.69
	-1.85	-2.11	+0.19	-0.89	-1.48	+1.13	+2.57	10.22
	1.2238	0.5617	1.0683	0.9848	1.0639	0.8277	1.1541	
$(A/A_i)_{r=9r_a}$	+.0010	+.0069	-.0025	-.0019	+.0040	-.0061	-.0079	0.0303
	+.0019	+.0187	-.0063	-.0058	+.0112	-.0161	-.0226	0.0826
	31.14	337.87	162.99	347.78	206.96	41.13	357.80	
$(\varphi^\circ)_{r=9r_a}$	-0.55	-0.35	-0.07	+0.13	-0.18	+0.35	-0.05	1.68
	-1.43	-0.97	-0.11	+0.34	-0.56	+0.99	-0.15	4.55

Table I.

Calculated non-dimensional wave amplitudes A/A_i and phase angles φ for plane time-harmonic (of period T = 480 sec.) incident waves around the Homma island in Fig. 3. Dimensionless radius r/r_a = 1, 2, 3, and 9. $\theta = 0^o, 30^o, \ldots, 180^o$. The values of phase angle φ are chosen in the interval $0^o \leq \varphi < 360^o$. For each of the 28 pairs of $(r/r_a, \theta)$ three results are given in a column. The upper number is the exact solution, the middle number is the difference with a sign between the exact solution and our FEM-solution Nr. I. The lower number is the difference with a sign between the exact solution and our FEM-solution Nr. II. The rightmost column contains for each line a summation of the absolute values of the differences mentioned above.

the area covering the shoal. The geometry is symmetrical and it could be modelled by a semi-infinite ocean, but the finite element grid (Fig. 4) is not symmetrical, so we have to introduce an infinite ocean model.

Exact solutions using an orthogonal collocation method and IDT wave theory for this problem have been published in tabular form earlier, see Jonsson et al. (1976) and Skovgaard and Jonsson (1981). Here an exact solution for a new wave period (T = 480 sec.) is given in Table I.

In Table I we have compared two finite element solutions (denoted by No. I and No. II) with the exact solution. FEM solution No. I is based on a very fine grid: $\Delta\theta = 6^o$, i.e. $\theta = 0^o, 6^o, \ldots, 360^o$, and $\Delta r/r_a = 0.1$ for $1 \leq r/r_a \leq 2$, and $\Delta r/r_a = 0.2$ for $2 \leq r/r_a \leq 3$, nmax = 16 (see Section 2). FEM solution No. II is based on a rather coarse grid: $\Delta\theta = 10^o$, i.e. $\theta = 0^o, 10^o, \ldots, 360^o$, and $\Delta r/r_a = 0.25$ for $1 \leq r/r_a \leq 3$, nmax = 11. The total number of elements is 1.800 and 576 in models No. I and II respectively.

Solution Nr. I was constructed in order to verify our model, i.e. verify the hybrid formulation, verify the functional, verify the discretization, and finally verify the implementation. Here the maximum distance (dimensionless with respect to local wave length, L_a = 31,648 m and L_b = 93,959 m) between neighbouring vertices of the triangular elements was of the order 0.05 for $r/r_a = 1$ and 0.04 for $r/r_a = 3$, i.e. minimum 20 Δs (see Fig. 4) per local wave length.

Solution No. II was constructed in order to measure the sensitivity of the finite element discretization. Here the maximum distance (dimensionless with respect to local wave length) between neighbouring vertices of the triangular elements was of the order 0.10 for $r/r_a = 1$ and 0.06 for $r/r_a = 3$, i.e. minimum $10\Delta s$ per wave length near ∂B and minimum $16\Delta s$ per wave length near ∂A.

Solution No. I has a maximum error in A/A_i of -0.0324 (corresponding to 1.37%) at $r/r_a = 1$ and $\theta = 0^o$ (point Q in Fig. 3, the centrepoint at the island in the shadow region). For the 28 results in Table I the mean error $(1/28\ \Sigma|\text{error}|)$ is 0.0082, or relative mean error $(1/28\ \Sigma|\text{error}|/(A/A_i)_{exact})$ 0.58%. The rightmost column informs us that the sum of the errors along $r/r_a = 1$ equals approximately the sum of the errors along the other three semi-circles r/r_a = 2, 3, and 9. Note that for all considered 28 points there is no distinct pattern of the signs of the errors. The maximum error in phases φ is -1.69^o and it is found at $r/r_a = 1$ and $\theta = 30^o$ (which is not where the maximum error in A/A_i was found). The mean error in φ $(1/28\ \Sigma|\text{error}|)$ is 0.54^o for the 28 results.

These results for solution No. I did not change when nmax was increased. This is in accordance with Skovgaard and Jonsson (1981), Fig. 24,

which showed that nmax $\gtrsim$ 12 was enough for $1 \leq r/r_a \leq 9$. To describe our *hybrid* finite element solution we present the calculated expansion coefficients α_o, α_n, and β_n for n = 1, 2, ..., nmax in Table II. First, in accordance with the reference mentioned above it was checked that the expansion coefficients in the table were in fact invariant to any increase in the number 'nmax'. Secondly, note that the largest β_n-coefficient is of the order of magnitude 10^{-15} (the magnitude of the largest α_n-coefficient is of the order of magnitude 1); this is in agreement with the fact that if a symmetrical grid had been used, all the calculated β_n-values should have been approximately zero, because for a semi-infinite ocean (Fig. 2) they are identically equal to zero.

Table II

Calculated expansion coefficients α_o, α_n, and β_n for n = 1, 2, ..., nmax = 16 in Eq. (1). T = 480 sec., FEM-solution No. I.

n	α_n		β_n	
	Re	Im	Re	Im
0	(-01)-1.9036	(-02)-3.7654		
1	+1.5557	(-01)-8.3137	(-15)+3.4083	(-15)-4.4021
2	(-01)+7.2245	(-01)+3.0857	(-16)+3.4004	(-16)-6.6716
3	(-03)-2.2846	(-02)+6.7557	(-16)-9.3783	(-16)-6.2251
4	(-03)-3.7408	(-06)-6.9968	(-16)+4.3754	(-16)+2.0117
5	(-09)+8.5146	(-04)-1.3050	(-17)+8.6204	(-18)+8.3134
6	(-06)+2.7177	(-12)+3.6930	(-18)-8.9236	(-18)+4.3720
7	(-16)-3.3380	(-08)+2.5711	(-19)-2.9753	(-19)+4.7180
8	(-10)+2.8321	(-19)-2.6609	(-19)+1.9747	(-20)+9.4608
9	(-20)-4.9453	(-11)+1.5208	(-20)+1.0105	(-20)+1.9679
10	(-13)-3.0731	(-21)-2.3659	(-21)+1.2234	(-22)+2.9296
11	(-22)-1.8402	(-15)-4.1857	(-22)-1.6817	(-23)+1.0816
12	(-17)+4.3363	(-23)-1.3715	(-24)+4.0399	(-23)+1.6757
13	(-24)-3.5198	(-19)+3.6025	(-24)+3.4282	(-24)+1.5503
14	(-21)-2.4754	(-26)+1.5796	(-25)+1.7842	(-26)+2.3390
15	(-26)-1.4705	(-23)-1.4367	(-27)+4.3157	(-27)+4.9126
16	(-26)+7.0580	(-29)+2.3355	(-28)+7.2292	(-28)+1.6390

We here ought to mention that the entire implementation was done on an IBM 3081 using double precision floating point numbers, which corresponds to approximately 16 floating point digits.

Solution No. II has a maximum error in A/A_i of -0.0981 (corresponding to 4.14%) at $r/r_a = 1$ and $\theta = 0^o$ (i.e. same point Q as for solution No. I). If we compare with Houston (1981), Figs. 7 and 9, which has a similar comparison but for another period (T = 120 sec.), it is seen that the largest error is found on the 'illuminated' side of the island (around point P in Fig. 3). From this we can draw the conclusion that the location of the largest error is very much dependent on the wave period. For the 28 results in Table I the mean error for A/A_i is 0.0223, or relative mean error 1.63% (which is about three times larger values than what was found for solution No. I). The rightmost column informs us that also for this solution (No. II) the sum of the errors along $r/r_a = 1$ equals approximately the sum of the errors along the other three semicircles r/r_a = 2, 3, and 9. Note that for all considered 28 points the signs of the errors in solutions No. I and II are the same, and the magnitude is roughly a factor three larger in case II than in case I.

The maximum error on the phases in solution No. II is -5.28^{o} and it is found in the same point as the maximum phase error in solution No. I. The mean error in φ in solution No. II is 1.55^{o} for the 28 results presented. Again this mean error is approximately about three times larger than the corresponding mean error for solution No. I. A calculation similar to case No. II with the same finite element grid but nmax increased from 11 to 20 was performed. Over the shoal there was no change in the solution for the five digits shown in Table I. However, for $r/r_a = 9$ minor changes in the errors were noticed, but these modifications were so small that the mean errors in A/A_i and φ given above did not change. Again, this is in agreement with Skovgaard and Jonsson (1981), where it was shown that for $r/r_a = 9$, nmax = 11 is just about too small to yield five digits of accuracy.

A contour plot of the A/A_i solution in model No. I is shown in Fig. 5. A three-dimensional plot of an instantaneous surface elevation around the island is shown in Fig. 6.

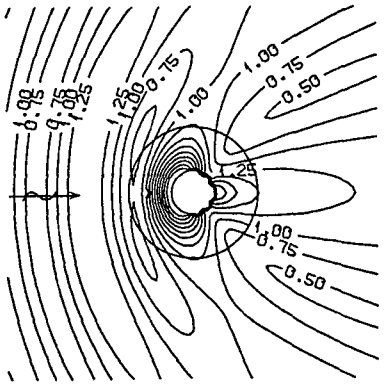

Figure 5. Contours for the relative amplitude around the Homma island, T = 480 sec. The interval between A/A_i-curves is 0.25.

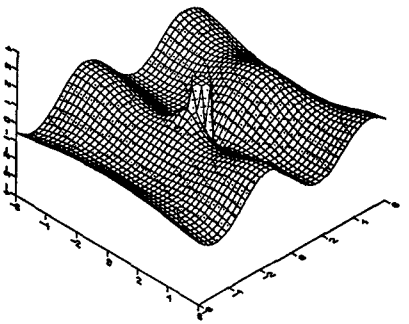

Figure 6. Relative surface elevation around the Homma island, T = 480 sec.

Finally, we stress that in this section we have investigated a rather difficult bottom geometry giving rise to combined shoaling, refraction, and diffraction in an infinite ocean model.

4. An Example of Absorption and Superposition: Rectangular Harbour

In this section we will demonstrate the effect of energy absorption along boundaries, the effect of obliquely incident waves, and finally the effect of superposition of incident waves of different angles and amplitudes. The presentation will be restricted to the simple harbour geometry shown in Fig. 7, left.

In Section 3 we considered an example of an infinite ocean (Fig. 1). Here we consider an example of a semi-infinite ocean (Fig. 2). The layout of the finite element grid and the location of the boundary ∂A between the finite element area A and the outer region R is given in Fig. 7, right. In Fig. 8 an enlarged sketch of the finite element grid around the tip of one of the breakwaters is shown.

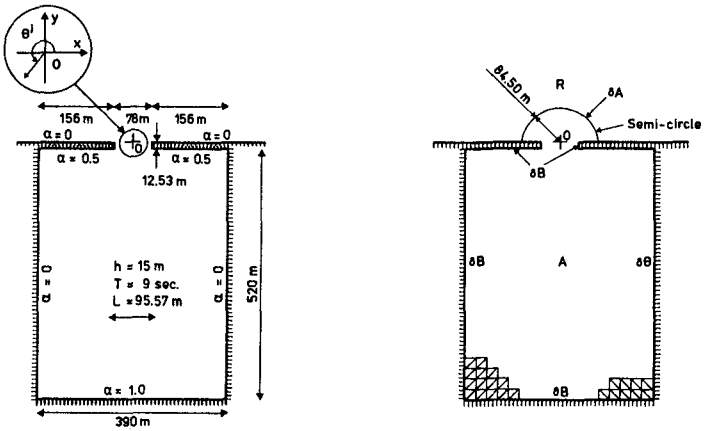

Figure 7. Left: Sketch of harbour geometry. Constant water depth in- and outside the harbour. Right: Sketch of finite element grid and boundary ∂A between finite element area A and semi-infinite ocean R.

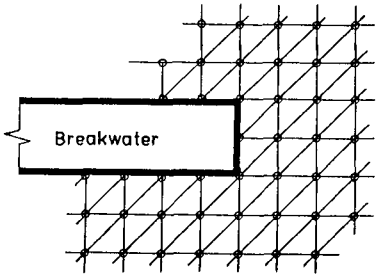

Figure 8. Detail of finite element grid around breakwater.

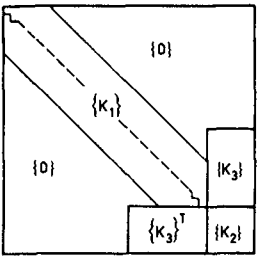

Figure 9. The coefficient matrix $\{K\}$ and its three submatrices $\{K_1\}$, $\{K_2\}$, and $\{K_3\}$.

The total number of nodal points in the finite element grid is 5,445 and the total number of elements is 10,556. Along the left and right boundaries inside the harbour there are 83 element sides, i.e. the short and long sides are 6.26 m and 9.02 m respectively. Along the innermost boundary of the harbour there are 60 element sides, i.e. the short and long sides are 6.50 m and 9.02 m respectively. In all the following figures a representative short wave period of T = 9 sec. has been used corresponding to a wave length in the entire area (constant water depth in the whole area for simplicity) of L = 95.57 m. This corresponds to a ratio of maximum side length in the elements to wave length of 9.02/95.57 = 0.0944 or minimum 10.6 element sides per wave length. This resolution is representative of what a practical engineer would use. Referring to the previous section one would expect a relative mean error in A/A_i and φ of

the magnitude 1 - 2% and 1^{o} - 2^{o} respectively. All figures were first calculated using nmax = 20. Hereafter all calculations were repeated with nmax = 24 (i.e. an increase of 4). No change could be detected in any figure.

The nodal points were numbered starting at the left-hand corner and going right on the innermost boundary of the harbour, i.e. the numbering was done along lines parallel to the x-axis (see Fig. 7, left). This principle has been used in the entire grid, also in the minor part of area A outside the entrance of the harbour. This was done to minimize the bandwidth in the coefficient matrix $\{K_1\}$, which is by far the largest of the coefficient matrix $\{K\}$, see Fig. 9.

The submatrix $\{K_1\}$ is stored in packed form giving it the dimensions: the number of nodal points (5,445) times the largest difference in nodal point numbers found in any element plus 1 (here 62 + 1 = 63), i.e. 5,445 x 63 = 343,035 complex numbers. The quadratic submatrix $\{K_2\}$ has the side length equal to the number of expansion coefficients, i.e. nmax + 1 (= 21), i.e. 21 x 21 = 441 complex numbers in the full matrix.

The submatrix $\{K_3\}$ has the dimensions of the largest difference in nodal point numbers of the nodes on ∂A (here equal to 283) times nmax + 1 (= 21), i.e. 283 x 21 = 5943 complex numbers.

The programming was done using the IBM OS PL/I Optimizing Compiler, release 4.0, see IBM (1981a) and IBM (1981b). All the programming was done in double precision, which with our machines is approximately 16 digits (8 bytes per real number and 16 bytes per complex number). The program was compiled and executed with VM/CMS on an IBM 3033 and with MVS/TSO on an IBM 3081 (16 M bytes of core memory on each machine). The CPU-times given below are from executions on the IBM 3081, which is a dual-processor machine. In the timings only one processor was used.

After testing, all debugging facilities were removed from the code and all programs were recompiled with the REORDER and OPTIMIZE(TIME) options. In the execution of this relatively modest harbour the whole code could reside in core memory during execution. For one single period (no superposition) the execution time was approximately 140 CPU-seconds (i.e. $2\frac{1}{3}$ min.) and the memory size 6 M bytes. Houston (1981) reported for a model of the same size (10,560 elements) an execution time of less than 1 min. on a CRAY-1. He used single precision in his FORTRAN program, which is approximately 15 floating point digits on a CRAY-1. When the CRAY-1 vector-computer is being used as a scalar computer, it is approximately 4 - 5 times as fast as a single processor of the scalar IBM 3081 computer. So we can conclude that our implementation is at least twice as fast as Houston's implementation. Note that the two implementations use approximately the same number of digits in the floating point calculations, viz. 16 and 15.

In Paper I, Figs. 3 and 4, an example of contours of relative amplitude and three-dimensional surface elevation at a specific time has been given in the case of normal incidence (in Fig. 7, left, $\theta^1 = 270^{o}$) and all boundaries being fully reflecting. To further illustrate these two figures we here show the relative wave amplitudes in three cross-sections parallel to the y-axis (see Fig. 7) in Fig. 10 and three cross-sections parallel to the x-axis in Fig. 11.

The first example is rather academic due to all boundaries being fully reflecting. In the following examples partial reflection is included in accordance with the α-values in Fig. 7, left. To be very precise, the α-value of 0.5 was used along the inner side of the breakwaters, around

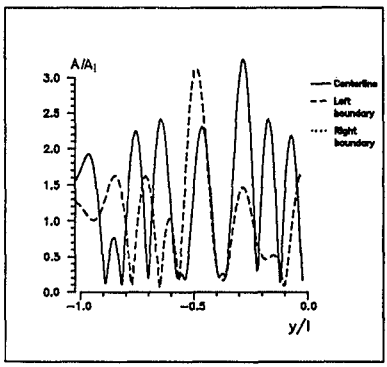

Figure 10. Relative wave amplitudes A/A_i for T = 9 sec. in three cross-sections: x = -195 m, 0 m, +195 m. All boundaries are fully reflecting, i.e. α = 0 everywhere. $\theta^i = 270^o$.

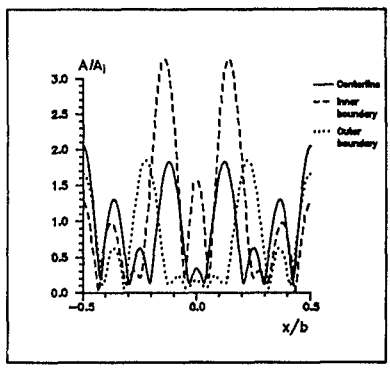

Figure 11. Relative wave amplitudes A/A_i for T = 9 sec. in three cross-sections: y = -532.53 m, -269.40 m, -12.53 m. All boundaries are fully reflecting, i.e. α = 0 everywhere. $\theta^i = 270^o$.

the tip of the breakwaters, and on that part of the outer side of the breakwaters that is inside area A.

In Figs. 12, 13, and 14 the results are shown for $\theta^i = 270^o$ with the absorbing boundary conditions.

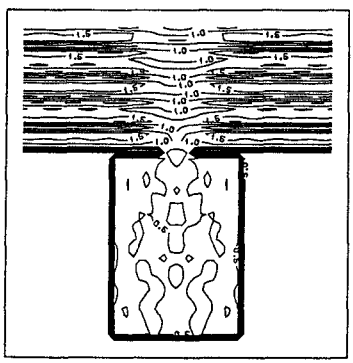

Figure 12. Harbour, contours of relative amplitudes A/A_i. T = 9 sec., $\theta^i = 270^o$. Partial absorption as defined in Fig. 7, left.

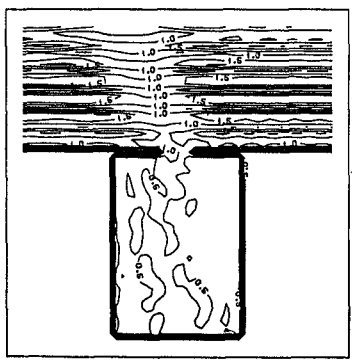

Figure 15. Same as Fig. 12, except that $\theta^i = 247.5^o$.

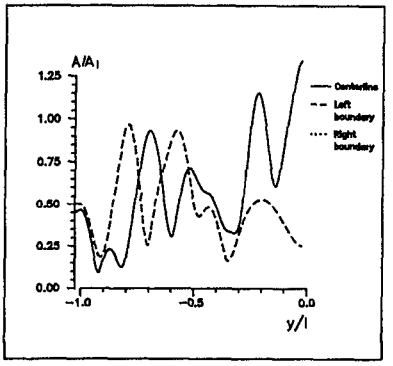

Figure 13. Same as Fig. 10, except for partial absorption as defined in Fig. 7, 1eft.

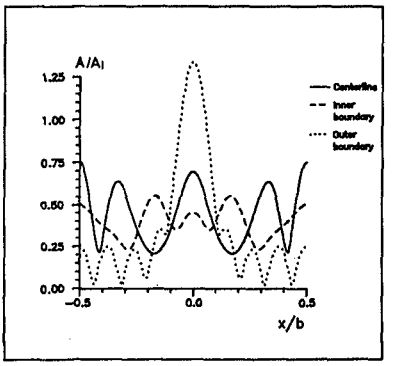

Figure 14. Same as Fig. 11, except for partial absorption as defined in Fig. 7, 1eft.

In Figs. 15, 16, 17, 18, and 19 the results are shown for $\theta^i = 247.5$ with absorbing boundary conditions.

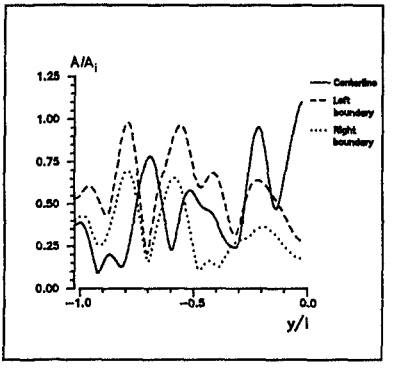

Figure 16. Same as Fig. 13, except that $\theta^i = 247.5^o$.

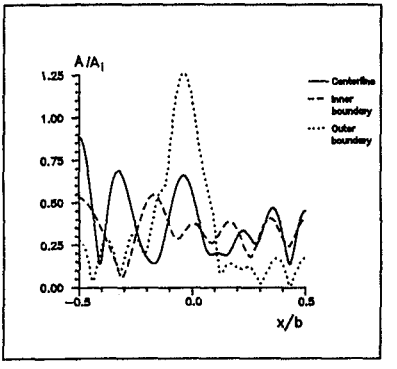

Figure 17. Same as Fig. 14, except that $\theta^i = 247.5^o$.

In Figs. 18 and 19 the results are shown for superposition of three different angles of incidence ($\theta^i = 225.0^o$, 247.5^o, and 270.0^o) with $A/A_i = 1/\sqrt{6}$, $\sqrt{2/3}$, $1/\sqrt{6}$ respectively (i.e. $A/A_i \approx 0.41$, 0.82, and 0.41). Note that $\Sigma(A/A_i)^2 = 1$ for the three incident wave systems.

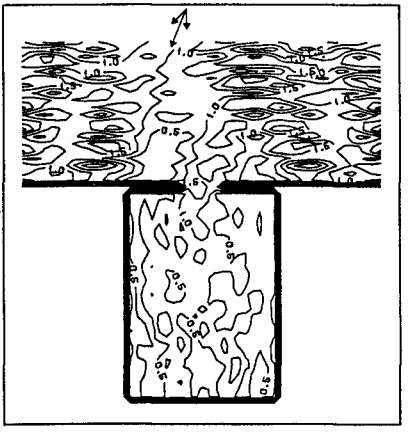

Figure 18. Harbour, contours of relative amplitudes A/A_i. Superposition of three incident wave systems, θ^i = 225.0°, 247.5°, and 270.0°. T = 9 sec. Partial absorption as defined in Fig. 7, left.

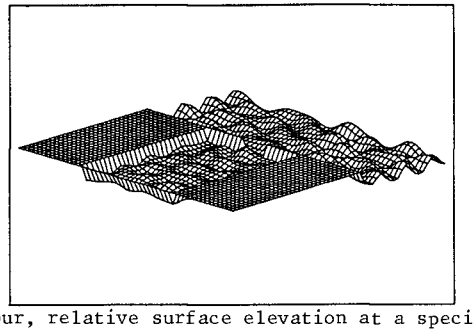

Figure 19. Harbour, relative surface elevation at a specific time corresponding to the example in Fig. 18.

5. Discussion and Conclusion for the Harbour Example

The first set of figures (Figs. 10, 11 and Figs. 12, 13, and 14) demonstrated in detail the effect of full reflection vs. partial absorption.

The next set of figures (Figs. 12, 13, and 14 and Figs. 15, 16, and 17) demonstrated in detail the effect of normal incidence vs. oblique incidence (same partial absorption in both cases).

The final set of figures (Figs. 15, 16, and 17 and Figs. 18 and 19) demonstrated in detail the effect of one direction of incidence with all the wave energy vs. the same amount of energy spread over three directions of incidence. The dominant direction in the superposed wave fields is the same as in Figs. 15, 16, and 17.

We notice that in the cases with normal wave incidence ($\theta^i = 270^o$) there is full symmetry, which is illustrated by Figs. 10 - 14.

The conclusions which can be drawn from all the sets of figures are not surprising: partial absorption diminishes the wave amplitudes drastically; the distribution of the same total wave energy among several directions has some diminishing effect on the wave amplitudes.

The execution time for calculating the wave field for a single period was earlier given to be $2\frac{1}{3}$ min. The code is still a research code, and if, in the future, consulting engineers are going to superpose many directions and many periods for each lay-out of the harbour geometry a more optimized code has to be developed.

A more promising alternative to decrease the execution time would be to develop and implement the model on a vector-processor like CRAY-X-MP, CYBER 205, NEC SX-2, FUJITSU VP-200, or HITACHI S-810. The first three machines are strictly FORTRAN-machines, but the last two have IBM-compatible sets of machine instructions and should therefore be able to run IBM PL/I, which has vector operations built into the language itself.

References

Berkhoff, J.C.W. (1972). "Computation of combined refraction-diffraction." Proc. 13th Coastal Engng. Conf., Vancouver, 1972, ASCE. New York, Vol. 1, Chap. 24, pp. 471-490.

Behrendt, L. and Jonsson, I.G. (1984). "The physical basis of the mild-slope wave equation." Proc. 19th Coastal Engng. Conf., Houston, 1984, ASCE. New York, in press. (Paper I.)

Chen, H.S. and Mei, C.C. (1974). "Oscillations and wave forces in an offshore harbor." Massachusetts Institute of Technology. Parsons Laboratory, Rep. No. 190.

Homma, S. (1950). "On the behaviour of seismic sea waves around circular island." Geophys. Mag., 21, pp. 199-208.

Houston, J.R. (1981). "Combined refraction and diffraction of short waves using the finite element method." App. Ocean Res., Vol. 3, No. 4, pp. 163-170.

IBM (1981a). "OS and DOS PL/I Language Reference Manual", Order number GC26-3977-0. White Plains, New York.

IBM (1981b). "OS PL/I Optimizing Compiler: Programmer's Guide", Order number SC33-0006-5. White Plains, New York.

Jonsson, I.G., Skovgaard, O. and Brink-Kjaer, O. (1976). "Diffraction and refraction calculations for waves incident on an island." J. Mar. Res., 34, pp. 469-496.

Skovgaard, O. and Jonsson, I.G. (1981). "Computation of wave fields in the ocean around an island." Int. J. Num. Meth. Fluids. Vol. 1, pp. 237-272.